Switchable SAW Resonators and Ladder Filters Composed of Interdigitated Combs

R. Alcorta Galván, Charles Croënne, Bertrand Dubus, B. Loiseaux, E. Eustache, M. Bertrand, A.-C. Hladky-Hennion

Switchable SAW Resonators and Ladder Filters Composed of Interdigitated Combs

R. Alcorta Galván, C. Croënne, B. Dubus, B. Loiseaux, E. Eustache, M. Bertrand, and A.-C. Hladky-Hennion

***Abstract*— This work presents the development of switchable SAW resonators fabricated on a $LiNbO_3$ substrate, which use the Electrical Bragg Bandgap concept to control the resonance frequency. The modification of the electrical condition of electrode arrays shifts their bandgap center frequency which in turn changes the effective cavity length and resonance frequency of the resonator. This method uses the electrodes already present in SAW devices, thus reducing the complexity of potentially tunable SAW components. In this paper, the electrodes which make up the cavity mirrors are connected into IDCP's (interdigitated comb pairs), reducing the necessary number of switches for operation. Finite Element Method (FEM) simulations are used to analyze resonator operation and design difficulties are discussed. Frozen (with no possibility of switching) and switchable versions of a chosen resonator structure are fabricated to experimentally showcase resonator operation. It is found that it is possible to design switchable SAW resonators which require a single switch and present a relative frequency jump of around 2.3%. Finally frozen single cell and 4-cell ladder filters are fabricated as a proof of concept of a switchable SAW filter.**

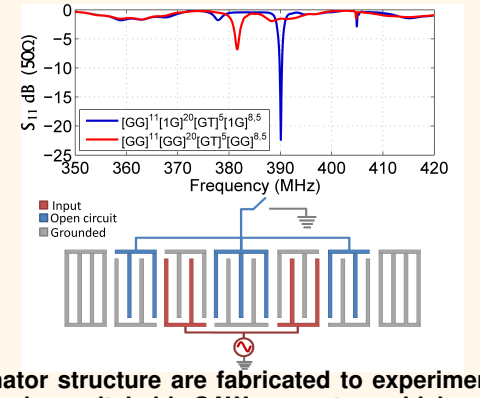

***Index Terms*— Electrical Bragg Bandgap, MEMS, Piezoelectricity, RF resonator, Single-Port SAW resonator, Tunable SAW device.**

I. Introduction

THE evolution of modern telecommunication standards imposes likewise an evolution of the hardware of radio frequency (RF) front ends to address an ever increasing number of frequency channels without increasing the footprint of the circuits. A solution that comes to mind is the use of tunable filters which can address several channels. In a 2015 article, Aigner reviewed the performance requirements and current state of acoustic wave filters which are used for the majority of filter functions in mobile phones, concluding that tunable filters were not likely to be a viable solution for years to come [1].

Nonetheless, several efforts to develop tunable SAW devices such as delay lines and resonators have been carried out. A first category relies on substrates whose properties are sensitive to external fields [2], [3] and a second on semiconductor-piezoelectric multilayers [4]–[6] which allow for control of SAW velocity by the giant acoustoelectric effect. Other examples closer to practical filter applications rely on the association of classical SAW resonators with MEMS capacitors that allow an adjustment of their antiresonance frequency and thus a control of the filter pass-band [7]–[10]. More recent efforts focus on "intrinsically switchable" devices based on ferroelectric substrates. High electrical fields can be used to polarize or depolarize the substrate which in turn controls the piezoelectric effect and response of the devices. Switchable SAW resonators [11] and switchable ladder FBAR filters [12], [13] have been proposed.

Another method was proposed in a very recent paper by Azarnaminy et al. [14], reconfigurable SAW resonators and ladder filters using monolithically integrated Vanadium oxide (VO_2) switches on an IHP substrate [15] were presented. The switching of the resonance frequency of the resonators (and pass-band of the ladder filters) is based on the use of a multi-electrode interdigital transducer [16] where certain electrodes are switched from a floating potential condition to a grounded condition.

In a recent paper [17], another way to achieve tunability of a symmetric single port SAW resonator was presented applying

Submitted for review July 5, 2024. This work was supported by the French Agence Nationale de la Recherche (FORMOSA Project No. ANR-18-ASMA-0003-01), the Agence Innovation Défense, and the Région Hauts-de-France.

R. Alcorta Galván, C. Croënne, B. Dubus and A.C. Hladky-Hennion are affiliated with Université de Lille, CNRS, Université Polytechnique Hauts-de-France, Junia, UMR 8520-IEMN, F-59000 Lille, France (e-mail: ricardo.alcorta.g@gmail.com).

B. Loiseaux, B. Matthieu and E. Eustache are with THALES Research & Technology France, Campus Polytechnique, 1 avenue Augustin Fresnel, F-91767 Palaiseau Cedex, France (e-mail: brigitte.loiseaux@thalesgroup.com).

Highlights

- **Proof-of-concept SAW resonators with switchable resonance frequency are designed, fabricated and characterized on wafer with a simple RF-probe-based commutation scheme.**
- **This work paves the way for the development of multi-channel SAW-based RF filters.**
- **Such devices have the potential to reduce the footprint and complexity of current SAW filter banks for RF applications.**

the Electrical Bragg Bandgap concept. The modification of the electrical condition of the mirror electrodes (without modification of the transducer), either connected to the electrical ground or set in a floating potential condition modifies the bandgap center frequency and thus the effective cavity length resulting in either a quasi-continuous resonance frequency shift or a resonance frequency jump. Independent electrical conditions are considered for each mirror electrode and thus a prohibitive amount of switches was necessary for practical operation.

In order to design SAW devices that can be practically switched, this work explores the switching of electrode arrays which are grouped into interdigitated comb pairs (IDCP) similarly to classic interdigital transducers (IDT). A comb makes reference to the series of connected electrodes presenting the same electrical condition. An interdigitated pair of combs not used as a transducer will be referred to as an IDCP. These resonators are used to make proof of concept of a switchable pass-band ladder filter. For this proof of concept, the choice is made to design the devices on a $LiNbO_3$ substrate with gold metallisations. This technological choice was made for practicality's sake and may not lead to optimal performance but will suffice for experimental verification.

This paper is divided into four main sections. The methodology section II lays out the theoretical framework for analyzing and designing the proposed switchable SAW devices as well as the geometry chosen to design switchable SAW resonators. The design approach is tested by FEM simulations resulting in a SAW resonator whose resonance frequency can be switched electrically.

Section III presents experimental verification of the designed devices using *frozen* (i.e. with no possibility of switching) and switchable single port SAW resonators. In subsection III-B the designed resonators are used to make proof of concept of a frozen ladder filter whose pass-band center frequency could be controlled if switches were appropriately integrated to control the electrical condition of the resonators. In section IV the results of the experimental realizations are discussed, as well as possible advantages, limitations and the still unresolved challenges of the proposed approach to design switchable SAW devices. Finally in section V, the conclusion, a brief summary of the results is presented as well as discussion of future works.

II. Methodology

A. Theory

1) Single Port SAW Resonator: In this section, the working principle of the single port SAW resonator (comprised of an IDT enclosed at both sides by Bragg mirrors) is discussed, based on the papers by Morgan and Hashimoto. In these papers, the P-matrix representation of IDT´s is leveraged to derive simple expressions that allow one to predict the resonance/antiresonance frequencies of the cavity [18], [19] and thus provide a very comprehensive explanation on the physics behind these devices. Based on these results the strategy for switching the resonance frequency of the resonators is described. Their findings are given here, limiting ourselves to the case of symmetric single port resonators with reciprocal propagation. The P-matrix representation of IDT´s is a 3x3 matrix linking incoming ($U_+(0)$ and $U_-(L)$) and outgoing ($U_-(0)$ and $U_+(L)$) acoustic waves at either side (1-D model) as well as the voltage (V) and current (I) at the electrical port. For a bidirectional and symmetric IDT, it can be written as [19]:

$$\begin{bmatrix} U_-(0) \\ U_+(L) \\ I \end{bmatrix} = \begin{bmatrix} p_{11} & p_{12} & p_{13} \\ p_{12} & p_{22} & p_{13} \\ -\chi p_{13} & -\chi p_{13} & p_{33} \end{bmatrix} \begin{bmatrix} U_+(0) \\ U_-(L) \\ V \end{bmatrix}. \quad (1)$$

The factor χ is a constant with a value of either 4 or 2 depending on the normalisation chosen for the different fields (either RMS or peak value). Special attention is drawn to the p_{33} parameter and in particular its real part, called the radiation conductance G_a. It can be shown that in frequency ranges where G_a is high, the electrical power injected to the IDT can be efficiently converted into SAW [18]. For an IDT placed between two identical mirrors modeled by a reflection coefficient Γ, the admittance of the resulting resonator for frequency ranges where $|\Gamma| \approx 1$, is written as [19]

$$Y = p_{33} + \frac{2\chi p_{13}^2}{p_{12} + p_{11} - \Gamma^{-1}} \approx j|p_{33}| \frac{sin\left(\frac{\phi_+ + \phi_\Gamma}{2} + \phi_I\right)}{sin\left(\frac{\phi_+ + \phi_\Gamma}{2}\right)}, \quad (2)$$

where $\phi_+ = arg\,(p_{11} + p_{12})$ can be regarded as a transmission phase of acoustic waves traversing the IDT. ϕ_Γ is the phase of the reflection coefficient of the mirrors and $\phi_I = \pi/2 - arg\,(p_{33})$ is a phase related to the electromechanical coupling. From eq. (2), one finds the resonance ($Y^{-1} = 0$) and antiresonance ($Y = 0$) conditions to be $\phi_+ + \phi_\Gamma = 2n\pi$ and $\phi_+ + \phi_\Gamma = 2(n\pi - \phi_I)$ (with $n \in \mathbb{Z}$) respectively.

The conditions for resonance/antiresonance can thus be summarized. The phase conditions between the mirror reflection coefficient and transducer transmission must be met in a frequency range where $|\Gamma| \approx 1$ and where $|p_{33}|$ (or the radiation conductance G_a) is large. If some conditions but not all of them are true any resonances would be highly attenuated. With this in mind, the working principle of the agile resonators

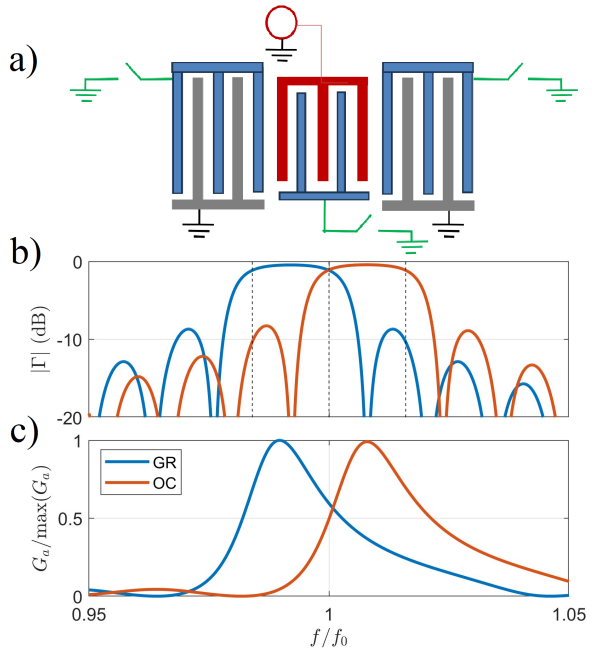

Fig. 1. a) Simplified schematic showing the basic concept of the switchable symmetric single port SAW resonator. The switches depicted in green will allow to change the mirrors and transducer from a GR to OC condition. The switching will both modify the range where $|\boldsymbol{\Gamma}| \approx \mathbf{1}$ (b) and the range where the transducer can excite SAW (where $\boldsymbol{G_a}$ is large) (c).

is schematized in Figure 1. To confer agility to the resonator (schematized in Figure 1 a) including schematic switches in green), changes of electrical conditions of electrodes will be considered for both the cavity mirrors and the transducer. The former will allow tuning the range where the mirrors confine waves in the cavity (Figure 1 b), while the latter will affect the IDT transmission phase and the frequency where radiation conductance is large (Figure 1 c). We consider two different electrical conditions, the grounded or GR condition (where electrodes are connected to the ground with electrical potential $V = 0$) and the floating potential or OC condition (where electrodes are left in floating potential and so the total charge under each electrode vanishes, $Q = 0$).

These changes will be leveraged to design single port SAW resonators presenting a single pronounced resonance/antiresonance frequency pair (a response of interest to use them as impedance elements in pass-band ladder filters) and which can be shifted in frequency by electrical switching.

2) Effect of the electrical condition on the resonator response: The mechanism through which the different parameters that determine the resonant frequency of the single port resonators will be modified is discussed in this section. In general, SAW devices for signal processing are made of periodic metallizations deposited on the surface of a piezoelectric substrate. The metallized sections of the surface present a different impedance to surface acoustic waves than the free surface of the substrate. This impedance mismatch causes reflections of incoming SAW, due to two competing effects. First, the deposited metal may locally constrain the substrate, or slow down the waves due to local increase of density in comparison to the free sections. Secondly, due to the piezoelectric effect, SAW also interact with the charges on the electrodes. Free charges in the metal in contact with the piezoelectric substrate can result in a discontinuity of the normal component of the electrical displacement field which can also cause partial reflection of SAW. These mechanical and electrical effects interact to cause dispersion of wave propagation on the infinitely periodic structure which depends on the electrical condition of the electrodes.

As a function of the electrical condition, dispersion is affected in two major ways. Firstly, the different phase velocity of SAW for each condition has an impact on phases ϕ_+ and ϕ_Γ. A finite size grating comprised of a certain number of electrodes can cause the waves to gain a different phase as they propagate through it (or are reflected from it) depending on the electrical condition of the electrodes. The resonance frequency of the device can then be controlled by changing the electrical condition and affecting reflection and transmission phases [17].

The second is the position of the bandgap frequency (range where condition $|\Gamma| \approx 1$ is met). In some frequency ranges, the individual reflections are in phase and forward propagating waves become evanescent. This effect is known as Bragg reflection. Bragg mirrors are designed in these specific frequency ranges to confine SAW into the cavity. The mechanical and electrical effects interact to form the bandgap and this interaction can be additive or on the contrary, result in a vanishingly small bandgap (this can be leveraged for example to design SPUDT's [20]). The modification of the electrical condition can cause a change of the bandgap frequency range, thus modifying the frequency where the cavity can support resonances and allowing us to design switchable SAW devices.

It is worth to mention that the frequency width of the bandgaps (for each condition, GR and OC), as well as their position relative to each other is dependent on the coupling of the SAW to the grating and the intrinsic electromechanical coupling of the substrate. This can limit the flexibility of the achievable modification of the resonance frequency and passband characteristics of the final filters to what is allowed by the substrate and electrode geometry chosen for the device.

This analysis is valid for an infinitely periodic series of individual electrodes with independent electrical conditions. Its validity for the interconnected electrodes forming the combs and IDT that will make up our resonator must be evaluated. For this, modal FEM simulations are used to calculate the bandgap edge frequencies. Fig. 2 a) shows a schematic of the FEM model. Two periods of the grating are modelled and a Bloch-Floquet periodic boundary condition is set between the left and right-most boundaries of the geometry. The study is focused on the bandgap since a modification of the bandgap frequency will be part of the strategy to design switchable resonators in sections II-B.3 and II-B.4, as well as the fact that the IDT used as transducers will only efficiently excite SAW in a relatively narrow frequency range close to the gap. Since two

electrodes are modelled, two different electrical conditions can be considered, one on each of the electrodes. The electrical potential of the first electrode is named V_1 and that of the second electrode V_2.

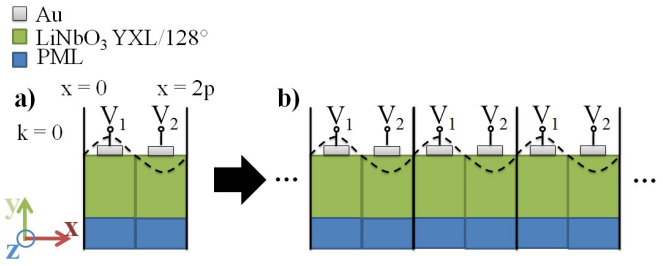

Fig. 2. a) Schematic of the FEM model used for modal simulations and calculation of the bandgap edges of the Rayleigh mode (found at $\boldsymbol{k}$ = 0) and b) the equivalent infinitely periodic structure.

Fig. 2 b) shows a schematic of the resulting infinite periodic grating simulated when $k = 0$ is imposed for the modal simulation, where the bandgap edges appear. The phase condition results in an infinitely repeating pair of electrodes with potentials V_1 and V_2. Using the hypothesis that the metal is a perfect conductor, this infinite periodic grating is equivalent to an infinite pair of interdigitated combs, each comb being connected to a busbar which prescribes the electrical boundary condition on the electrodes of each period. Two electrical conditions can be imposed on the electrodes: each electrode is either grounded with null electrical potential ($V = 0$) or in floating potential for which the total charge on the electrode cancels out ($Q_{total} = 0$) and the potential is to be determined. Because the electrical potential is defined to within a constant only two distinct types of electrical conditions imposed on the comb pair must be considered : $V_1 = V_2$ or $V_1 \neq V_2$. When both combs are connected to the ground, the grating corresponds to a $V_1 = V_2$ condition and likewise when the combs are connected together and left in floating potential. When one of the combs is connected to the ground and the other left in a floating potential condition or when both the combs are in floating potential, the grating corresponds to the $V_1 \neq V_2$ condition.

Indeed, modal simulations show that the bandgap edges for the $V_1 = V_2 = 0$ (both combs grounded) as well as the $V_1 = V_2$ and $Q_1 + Q_2 = 0$ (both combs of the pair interconnected and left in floating potential) conditions are those of a GR mirror. On the contrary, for the $V_1 \neq V_2$ and $Q_1 = 0$ or $Q_2 = 0$ conditions (either both combs are in floating potential or one of the combs is in floating potential and the other one connected to the ground), the bandgap edges are those of an OC mirror. Thus, in theory, a single switch could be used to change large interdigitated comb mirrors from a GR condition to an OC condition.

It is worth it to note that it is only at $k = 0$ at the bandgap edges that the interdigitated combs are strictly equivalent to an array of independent OC electrodes. Because of this we can expect the Bragg bandgaps to be present at the same frequencies for both independent electrodes and IDCP's. A detailed analysis of the way in which the connection of electrodes into IDCP's impacts dispersion of SAW is outside of the scope of this paper and will be treated at a later date. The impact of the connection of electrodes into finite size IDCP's will be analysed directly in the electrical response of the resonators. Due to their finite size the IDCP's will present a supplementary reflection of waves referred to as SAW electrical regeneration which will be discussed in detail in section II-B.3. This effect is de-facto taken into account in the full-wave FEM simulations.

TABLE I
GEOMETRICAL PARAMETERS OF THE RESONATOR.

	Period	a/p	Electrode thickness h	Number of electrodes
Transducer	4.74 μm	0.49	130 nm	17
Mirrors	4.87 μm	0.455	130 nm	72

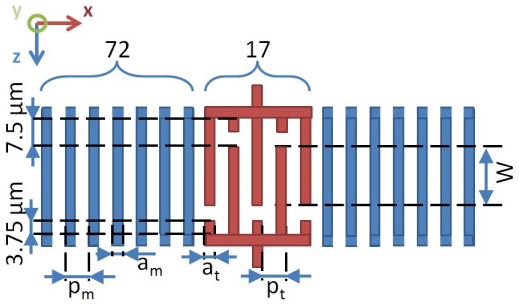

Fig. 3. Schematic description of the single-port resonator made of a transducer (red electrodes) between two Bragg mirrors (blue electrodes).

B. Design of Switchable Resonators

1) Base Geometry: In this section, the geometry of the resonator to be studied [17] is presented (Table I and Fig. 3). The base structure is a symmetric single-port SAW resonator, comprised of an interdigitated transducer enclosed by two Bragg mirrors. The width of the electrodes is denoted a. The acoustic aperture (electrode length along z) is set to W = 200 μm. The electrical conditions of the left and right mirrors are also symmetric. The distance between the mirrors and the transducer is set to zero.

The studied resonators are fabricated on a $LiNbO_3$ YXL/128° substrate with Au metallisations. Material parameters used are given in the appendix. Modal simulations show that the bandgap of the mirrors for the Rayleigh mode when the electrodes are set to an OC condition is present in the [381.6, 387.1] MHz frequency range whereas when they are switched to the GR condition, the bandgap is present in the [375.5, 381.6] MHz frequency range. These bandgaps are adjacent, sharing a common edge at 381.6 MHz. Thus a change of the electrical condition of the mirrors will result in a jump of the range where resonances can occur. The resulting bandgaps also have similar width and therefore the mirror will have a similar reflection coefficient for both electrical conditions.

The central IDT has a relatively broad -3dB bandwidth (in terms of radiation conductance) of around 28 MHz and is centered at around 379 MHz close to the common edge of

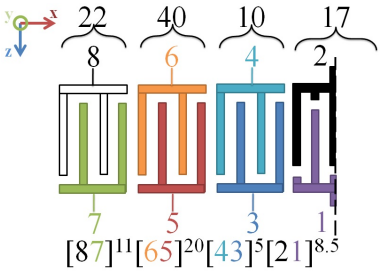

Fig. 4. Schematic of the chosen partition of the resonator electrodes into combs, only the left half of the device is presented.

the OC and GR bandgaps of the mirrors. The broad -3dB passband is a consequence of the low number of electrodes in the IDT which also causes the transmission phase ϕ_+ to evolve slowly so that the phase condition for resonance will be met at the lower edge of the GR bandgap and near the upper edge of the OC bandgap.

A shear horizontal (SH) SAW mode can also propagate on this substrate/metallisation combination. Since this SH mode is not properly confined to the surface, it results in relatively inconsequential resonances on the resonator response (present in the admittance curves on the following sections at around 403 MHz) when compared to those resulting from the Rayleigh mode. It is worth mentioning that the gold metallizations exhibit relatively high mechanical losses [21]. These losses mostly affect the quality factor of resonances. Thus, lossless COMSOL simulations are used throughout this paper as guidelines for analysis even though they are not representative of the final device performance.

2) Division of mirror electrodes into IDCP's: The mirrors are divided into interdigitated comb pairs (IDCP´s) and the single port resonator response is calculated numerically by FEM simulations for different conditions of these mirror IDCP's. The piezoelectric problem is solved in the substrate which is enclosed by Perfectly Matched Layers (PML'S) to limit the simulation domain. All the electrodes on the surface of the substrate are modelled as classical isotropic elastic materials. The interaction between the electrodes and the substrate is modelled by applying electrical boundary conditions on the substrate-electrode boundaries. To reduce model size, a symmetric boundary condition is used for plane Oyz and only half of the resonator is simulated. Additionally, only a thin slice of the device on the z direction is modelled, and a periodic boundary condition is set in order to simulate an infinite acoustic aperture resonator.

In order to simplify the discussion of the different mirror electrical conditions, a shorthand notation is defined for the configurations. Since the structure is symmetric, it is sufficient to describe the electrical state of each comb of one of the mirrors and that of the central (at the symmetry plane) combs initially corresponding to the transducer.

- Grounded combs are represented by the letter G.
- Single floating potential (open circuit) combs are represented by the letter O.
- Combs which are interconnected and left in floating potential are represented by numbers. Combs with the same number are interconnected.
- Lastly, the letter T is used to identify the comb used as the input port (transducer).

The combs are described by pairs enclosed by square brackets. One character is used to describe the electrical condition of each comb. The first pair enclosed by brackets represents the comb pair furthest from the center, the following bracket the following comb pair towards the center and so on. An exponent is added to each square bracket to indicate the number of repetitions of the pair of electrodes in the comb pair. The first character inside each bracket pair describes the condition of the comb to which the electrode furthest from the center belongs. For the considered resonators, the electrical condition of the left mirror is specified, as well as the combs corresponding to the central IDT. Finally, to represent IDT´s with an odd number of electrodes in total, the notation $[AB]^{n+0.5}$ is used. This indicates that the pattern is repeated n and a half times, and so the first and last electrodes of the IDT belong to the same comb. With this convention, the resonator of figure 4 for which the central comb pair is used as the transducer and the mirror combs are all grounded is written $[GG]^{11}[GG]^{20}[GG]^{5}[TG]^{8,5}$.

3) Agility by Mirror Switching: In this section, the agility is studied when only the mirror electrical conditions are modified. First, the 10 and 40-electrode IDCP's are combined to form a 50-electrode IDCP (see Fig. 4, with combs 3 and 5 interconnected, as well as combs 4 and 6). In this configuration, a large section of the mirror can be switched between the GR and OC bandgap using a single switch keeping complexity to a minimum. The responses of the resonator for various conditions of the mirrors are presented in Fig. 5 a-d). Based on the discussion in section II-A.2, many of the mirror electrical conditions are equivalent. These responses are grouped together to showcase the equivalence of different electrical conditions, many of the curves in each graph being practically confounded with one another. A much weaker resonance/anti-resonance is found due to the SH-SAW mode centered at 402.55 MHz for all electrical conditions. This mode is barely affected by the electrical condition of the mirrors.

Four distinct electrical conditions are possible with the chosen mirror division. From a-d) respectively,

- Both mirror IDCP's have a $V_1 = V_2$ condition.
- The 50 and 22 electrode IDCP's have a $V_1 \neq V_2$ and $V_1 = V_2$ conditions respectively.
- The 50 and 22 electrode IDCP's have a $V_1 = V_2$ and $V_1 \neq V_2$ conditions respectively.
- Both mirror IDCP's have a $V_1 \neq V_2$ condition.

The reflection coefficient inside the bandgaps is caused by Bragg reflections and depends heavily on the size of the mirror. The 22-electrode IDCP is very short and so by itself it doesn't confine SAW very effectively, hence the main resonance frequency (the one with the highest quality factor)

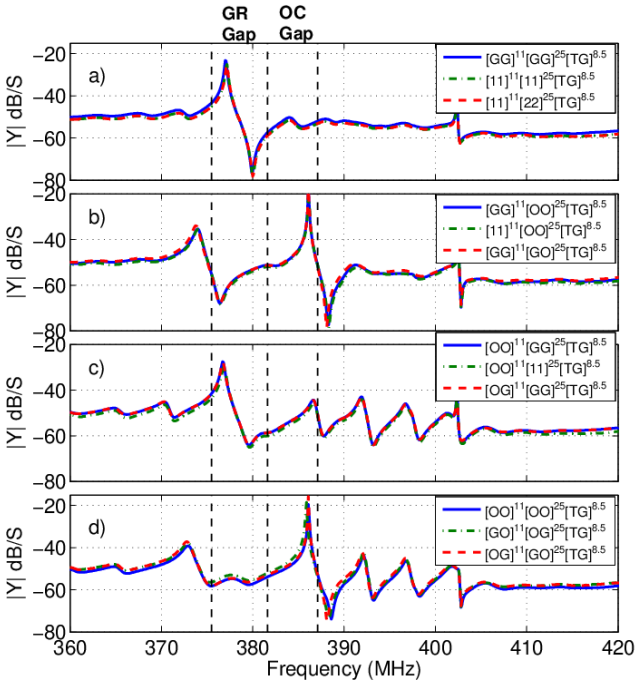

Fig. 5. Admittance amplitude in decibels ($20\text{Log}_{10}(|\boldsymbol{Y}|)$) for multiple electrical conditions of the mirror combs. The different cases are separated into four sets (a-d) showcasing that several electrical conditions are equivalent. The vertical dashed lines mark the edges of the GR and OC bandgap.

depends on the electrical condition of the 50-electrode IDCP. When it is grounded, Fig.5 a and c) the main resonance is present in the GR bandgap. In Fig.5 a) the whole mirror is grounded and thus the resonance is of much better quality than for case c). When the 50-electrode IDCP is in OC condition (Fig.5 b and d), the main resonance is found in the OC bandgap.

In figures Fig.5 b-d), the presence of floating potential IDCP's causes extra parasitic resonances outside of the bandgap due to SAW electrical regeneration. This effect was discussed by Hashimoto in the context of triple transit echo [24]. The concept of SAW electrical regeneration can be understood by considering a device comprised of two acoustically coupled IDT´s with one open port (an IDT in floating potential condition). When the signal is injected through the transducer, it excites the floating potential IDT through either electrostatic coupling or launching of SAW. Since a floating potential condition is imposed, this excitation is entirely "electrically reflected" (or regenerated) back into the cavity. A potential appears in the comb which launches SAW back towards the central transducer.

In Fig.5 b) it is the resonance with lower quality factor at 373.9 MHz, and in figure Fig.5 c) the low quality resonances at 392 MHz and 396.8 MHz (the weak resonance inside the OC bandgap is attributed to Bragg reflections from the 22-electrode IDCP). In figure Fig.5 d) the parasitic resonances from cases b) and c) are still present, with a response close to a linear superposition of the two individual cases. The analysis of section II-A.1 tells us that for the cavity to

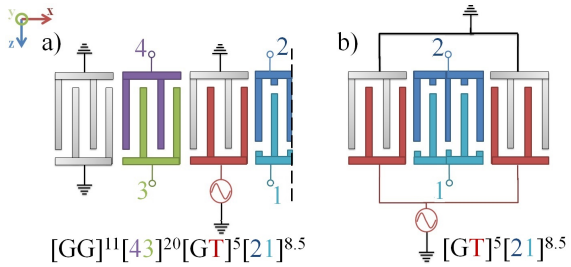

Fig. 6. Schematic of the switchable resonator a) (left half) and of the switchable transducer b) studied in this section.

resonate the mirrors must have a high reflection coefficient ($\Gamma \approx 1$) . This means that electrical regeneration from IDCP's can be thought of as an addition to the reflection coefficient, extending its working frequency from the original bandgaps. Although a main resonance frequency jump can be seen by passing from cases a) to b) or d), the admittance for cases b) and d) presents undesired out of band resonances which would result in a degraded response if these resonators were to be used to build pass-band filters. Following the concept of section II-A.1, along with switching cavity mirrors, tuning of the transducer is implemented in the following section to avoid exciting spurious resonances.

4) Agility by Mirror Switching and Transducer Tuning: In order to improve the response of the resonator, one of the 5-electrode combs contiguous to the central IDT is used as an entrance port. The resulting resonator is schematized in Fig. 6 a) (left half), and the split transducer in Fig. 6 b) (full transducer without mirrors). The basic idea behind this type of split transducer configuration is that its properties can be slightly modified or tuned by changing the electrical condition of the IDCP located between its two halves, which then serves as a type of coupler.

In order to show the benefits of using the commutable transducer, Fig. 7 shows the radiation conductance (real part of the admittance) of the original transducer (a) as well as of the commutable transducer for all electrical conditions of the center IDT (b), in the absence of any other mirror.

As previously discussed, the original transducer ($[TG]^{8.5}$) has a wide -3dB pass band and thus a low frequency selectivity, leading to the excitation of several resonances when integrated into the cavity. The new transducer presents three high radiation conductance lobes for all coupler connection cases. The appearance of three lobes is a result of the split of the transducer into two halves which interfere constructively or destructively.

The center lobes are sharper, presenting a -3dB band of around 10 MHz compared to 28 MHz for the original transducer. Additionally, it can be seen that for a $V_1 = V_2$ type condition on the central coupler (cases $[GT]^5[GG]^{8.5}$ and $[GT]^5[11]^{8.5}$), the maximum of the lobe is present around 379 MHz. Switching to electrical conditions presenting the OC bandgap (cases $[GT]^5[GO]^{8.5}$, $[GT]^5[OG]^{8.5}$, and $[GT]^5[OO]^{8.5}$) causes a shift of the lobes by a few MHz to around 385 MHz. This switching could be seen as modifying the velocity of

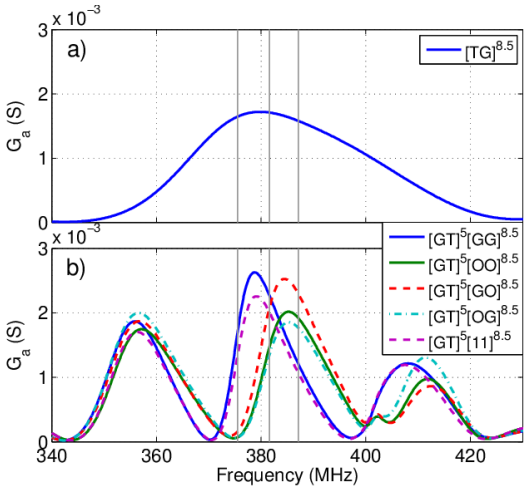

Fig. 7. Radiation conductance calculated by FEM simulation of the original transducer a), and the commutable transducer for different electrical condition of the center combs b). The vertical greylines mark the edges of the GR and OC bandgap.

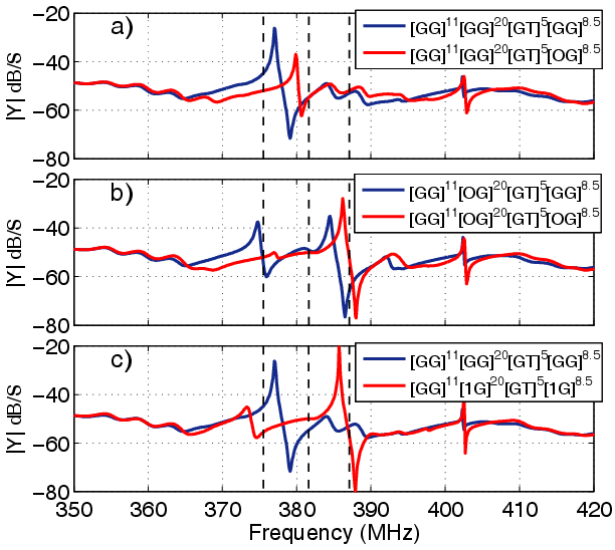

Fig. 8. Admittance of the split transducer resonator for different electrical conditions. a) All mirror IDCP's are grounded, b) the 22-electrode IDCP is grounded while the 40-electrode comb pair is set to an $[\boldsymbol{OG}]^{\boldsymbol{20}}$ condition. In Fig. c) the floating potential comb used to control the transducer and the one used to control the mirror are interconnected to reduce the number of switches necessary. The vertical dashed lines mark the edges of the GR and OC bandgaps.

SAW and thus the effective length of the coupler separating the two halves of the transducer resulting in the shifting of the passband of the IDT. This shift provides a switch of transducer operation from the GR bandgap to the OC bandgap. All cases with an OC coupler exhibit similar shifts. However, case $[GT]^5[GO]^{8.5}$ presents the highest radiation conductance peak. This is accredited to the fact that all the active electrodes are surrounded by electrodes connected to the ground and so an important potential difference between all active electrodes and their neighbors can be developed to launch SAW efficiently.

Fig. 8 a) and b) presents the resonator response for different conditions of the mirrors and split transducer. The red curves correspond to cases where the central coupler presents a $[OG]^{8.5}$ condition whereas for the blue curves both combs are grounded ($[GG]^{8.5}$). In Fig. 8 a) the mirrors are grounded, in Fig. 8 b) one comb from each pair is floating so both sections have the OC bandgap.

In both cases, a shift of the resonances towards higher frequencies can be seen. In Fig. 8 a) the mirrors work in the GR bandgap and the response of the resonator for case $[GG]^{11}[GG]^{20}[GT]^5[GG]^{8.5}$ is hence similar to that of case $[GG]^{11}[GG]^{25}[TG]^{8.5}$ (Fig. 5 a) in which the mirrors are grounded and the center transducer is used. The resonance is however slightly attenuated due to the fact that the entrance port is located further from the center and thus a reduced number of mirror electrodes is used to confine energy. In Fig. 8 b) one of the 20-electrode combs is left in floating potential. Bragg reflections occur in the OC bandgap for a majority of the mirror and thus for both conditions of the transducer the main resonance occurs inside this frequency band. For case $[GG]^{11}[OG]^{20}[GT]^5[GG]^{8.5}$ a parasitic resonance is present around 375 MHz due to SAW regeneration from the 40-electrode IDCP in OC condition. In case $[GG]^{11}[OG]^{20}[GT]^5[OG]^{8.5}$, this parasitic resonance is highly attenuated since a minima of radiation conductance for the $[GT]^5[OG]^{8.5}$ (Fig. 7 b) transducer is present in this frequency range. The response of the resonator for this case indeed presents a single main resonance and is thus of interest for a practical application.

Consequently, a change between the $[GG]^{11}[GG]^{20}[GT]^5[GG]^{8.5}$ (Fig. 8 a), blue curve) and $[GG]^{11}[OG]^{20}[GT]^5[OG]^{8.5}$ (Fig. 8 b), red curve) conditions results in a jump of the main resonance/antiresonance frequencies of the cavity without introducing significant secondary resonances.

To switch between these two states, three switches are needed (one per mirror and one for the central coupler). To reduce this number, a simplification of the resonator is made by interconnecting the mirror and transducer combs so that they can be switched simultaneously. Fig. 8 c) presents the admittance of the resonator for the resulting $[GG]^{11}[GG]^{20}[GT]^5[GG]^{8.5}$ and $[GG]^{11}[1G]^{20}[GT]^5[1G]^{8.5}$ conditions. Even after connecting the mirror and coupler combs, case $[GG]^{11}[1G]^{20}[GT]^5[1G]^{8.5}$ still presents the OC resonance from case $[GG]^{11}[OG]^{20}[GT]^5[OG]^{8.5}$. Interestingly the resonance seems to be slightly improved by the interconnexion of the combs (higher maxima and lower minima at the resonance and antiresonance frequency, and a much flatter admittance for frequencies between 390 and 400 MHz), the only downside being a small parasitic resonance at around 374 MHz.

It must be said that although so far the choice of which comb to set to a floating potential condition in order for a pair to present the OC bandgap has been of little importance (only marginal differences between several connection cases in Fig. 5 and Fig. 7), this choice becomes crucial for the interconnection of the central coupler and the mirror combs. Fig. 9 shows the admittance of the resonator for different interconnections between the center comb pair that make

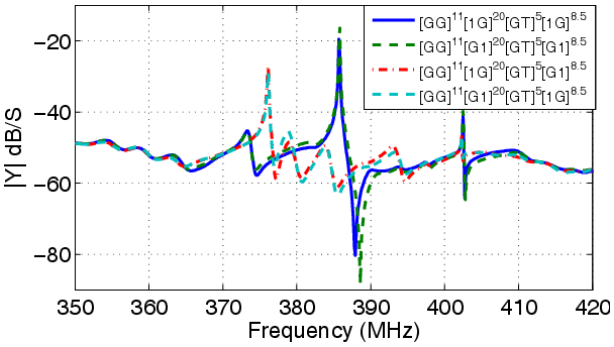

Fig. 9. Admittance of the resonator for different interconnections between the coupler and mirror combs such that a single switch is necessary to set the resonator to the $[\boldsymbol{GG}]^{\boldsymbol{11}}[\boldsymbol{GG}]^{\boldsymbol{20}}[\boldsymbol{GT}]^{\boldsymbol{5}}[\boldsymbol{GG}]^{\boldsymbol{8.5}}$ condition.

up the coupler and the 40-electrode IDCP's in the mirrors. Two of the interconnections allow the preservation of the OC resonance while the other two do not. In order to explain which interconnection is permissible to keep the OC resonance, the standing wave pattern near this resonance frequency should be considered. It is well known from the study of SAW devices by the coupling of modes method that the field inside the resonator can be expressed as an envelope of slowly varying amplitude modulated by a sinusoidal term of spatial periodicity close to that of the grating [25]. In each IDCP, the electrodes from one comb are spatially shifted by half a wavelength from those of the other and so they exhibit opposite polarities. For the two cases that preserve the OC resonance, the interconnected combs are separated from each other by an even number of electrodes (half wavelengths). Thus, they present an equal polarity, meaning that the voltage on both the combs evolves in phase. Because of this, the combs interact marginally despite their electrical connection. On the contrary, for cases $[GG]^{11}[1G]^{20}[GT]^{5}[G1]^{8.5}$ and $[GG]^{11}[G1]^{20}[GT]^{5}[1G]^{8.5}$, the potential of the combs that are interconnected would otherwise evolve in phase opposition and thus the response of the resonator is highly perturbed by their connection.

As pointed out before, for cases $[GG]^{11}[1G]^{20}[GT]^{5}[1G]^{8.5}$ and $[GG]^{11}[G1]^{20}[GT]^{5}[G1]^{8.5}$ (Fig. 9), the resonance is enhanced with respect to that of case $[GG]^{11}[OG]^{20}[GT]^{5}[OG]^{8.5}$ (Fig. 8 b), red curve) for which the mirror and coupler floating potential combs are not interconnected. This result suggests that the interconnection modifies the mode shape in the cavity such that more energy is focused in the combs used as transducers. In the literature the only similar structure (using interconnected combs) found by the authors was a "Connected IDT" RFID SAW tag proposed by Floer et al. [26] in which the interconnection, in contrast to our case, improves the time domain response of the RFID tag.

Case $[GG]^{11}[1G]^{20}[GT]^{5}[1G]^{8.5}$ is retained for fabrication of a switchable resonator in the following section. A 2.2% resonance frequency jump is expected by setting this resonator to a $[GG]^{11}[GG]^{20}[GT]^{5}[GG]^{8.5}$ condition (simulated response shown in Fig. 8 c).

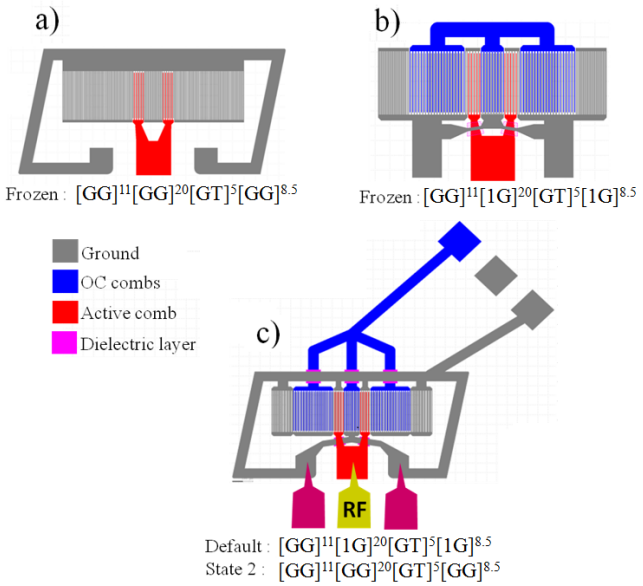

Fig. 10. Schematics of the fabricated resonators. FROZEN (no switching possible) devices for comparison (a) and (b) as well as switchable device "Switch 1".

III. Results (Experiments)

A. Fabrication and measurement of a switchable resonator by transducer and mirror switching

Fabrication is carried out as follows: metallization patterns are defined by e-beam lithography (Nanobeam Nb4 equipment) using a PMMA C7 resist on a 4 in. $LiNbO_3$ YX/L 128° substrate wafer. A 130 nm thick layer of gold is then deposited by electron gun evaporation before the resist liftoff. Extra fabrication steps are added to the fabrication process to allow for crossings of independent metallic strips, namely a deposition and patterning of dielectric bridges (shown in magenta in Fig. 10 b and c), followed by a second metallization process. Additional characterization shows that, for the frequency range of interest, these dielectric bridges act like simple capacitances with a weak loss tangent. Fig. 10 shows the fabricated resonators. The resonators in Fig. 10 a) and Fig. 10b) are frozen, i.e. with no possibility of switching and correspond to electrical conditions $[GG]^{11}[GG]^{20}[GT]^{5}[GG]^{8.5}$ and $[GG]^{11}[1G]^{20}[GT]^{5}[1G]^{8.5}$ (Fig. 8 c) respectively.

In contrast, the resonator in Fig. 10 c) can be switched. To switch the electrical condition, three extra pads are added (seen in the top right corner) as well as strips connecting the floating potential combs (blue) and ground (gray) to them. To switch the electrical condition of the combs, a GSG probe can be connected to the three extra pads. The internal connection between the G tips of the probe electrically connects the top and bottom-most pads. This resonator (Fig. 10 c) named "Switch 1" has two states: a default state without the extra GSG probe placement which corresponds to the $[GG]^{11}[1G]^{20}[GT]^{5}[1G]^{8.5}$ electrical condition, and a second state (State 2) achieved by lowering the extra GSG probe which corresponds to the $[GG]^{11}[GG]^{20}[GT]^{5}[GG]^{8.5}$ condition.

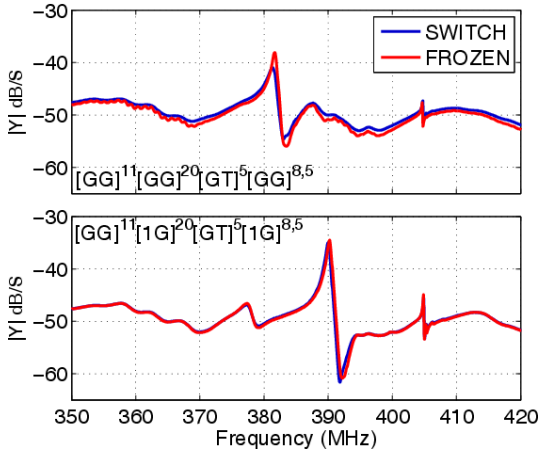

Fig. 11. Measured response of the frozen resonators (Fig. 10 a) and b) as well as the two states of resonator "Switch 1" (Fig. 10 c) for comparison.

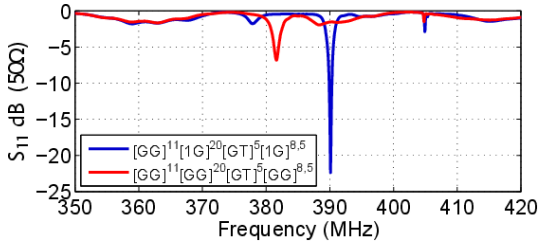

Fig. 12. Measured S parameter of the "Switch 1" resonator (Fig. 10 c) for both electrical conditions.

For measurement, a second GSG probe is placed on the input port pads and connected to a VNA. On-wafer calibration is used. Fig. 11 shows the measured response for both frozen resonators as well as resonator "Switch 1" for the different electrical conditions. Fig. 12 shows the measured S_{11} parameter of the switchable resonator for both electrical conditions. A clear jump of the resonance frequency can be seen.

A comparison of the measured (Fig. 11) and simulated (Fig. 8 c) responses shows the aforementioned attenuation of all resonances caused by the mechanical losses in the metallizations as well as a shift of the whole spectrum by around 4 MHz to higher frequencies which is likely caused by inaccuracies of the material parameters used in the simulations. Nonetheless, the main characteristics identified in the FEM simulations are present for each case, namely both the Rayleigh and SH resonances. For case $[GG]^{11}[1G]^{20}[GT]^{5}[1G]^{8.5}$ the response of both the switchable and frozen cases are almost identical whereas for case $[GG]^{11}[GG]^{20}[GT]^{5}[GG]^{8.5}$ the resonance for the "Switch 1" case is slightly attenuated. The spectrum also presents a slightly higher level on the whole frequency band which means an increased static capacitance. These effects are attributed to a capacitive effect between the floating potential combs and the ground through the dielectric layers of the bridges as well as from the switching of the electrical condition by the GSG probe.

By switching the electrical condition of the combs a jump of the main resonance frequency of the resonator by 2.23% (from 381.4 to 390 MHz) is observed. The characteristics of the measured (exp.) and simulated (sim.) electrical response of the resonator in terms of impedance at the resonance/anti-resonance frequencies are summarized in Table II. f_c is the center frequency (arithmetic mean between resonance and anti-resonance frequencies), Δf the difference between the resonance and anti-resonance frequencies, $|Z_r|$ and $|Z_{ar}|$ the magnitude of the impedance at resonance and anti-resonance frequencies respectively, and finally Q_r and Q_{ar} are the calculated quality factors at resonance and anti-resonance frequencies respectively. Lakin's formulation is employed, Feld et al. showed that it's equivalent to their general formulation at the resonance and antiresonance frequencies [33]. A forward difference method (with a step of 0.05 MHz) is used to approximate the derivative followed by linear interpolation to find Q at the identified resonance frequencies.

TABLE II
RESONANCE/ANTI-RESONANCE CHARACTERISTICS OF THE SWITCH 1 RESONATOR IN TERMS OF IMPEDANCE.

	f_c (MHz)	Δf (MHz)	$\|Z_r\|\Omega$	$\|Z_{ar}\|\Omega$	Q_r	Q_{ar}
Default (exp.)	390,95	1,9	56,10	1206,4	510.5	364.4
State 2 (exp.)	382,25	1.7	111,81	537,03	229.2	171
Default (sim.)	386.8	2.2	9.477	10416	4036.6	1341.2
State 2 (sim.)	378.05	2.1	20.57	3809.7	1730.8	909.2

$$Q_r = 0.5 f_r abs\left(\partial\phi_z/\partial f\right)|_r$$
$$Q_{ar} = 0.5 f_{ar} abs\left(\partial\phi_z/\partial f\right)|_{ar}, \quad (3)$$

with ϕ_z being the phase of the impedance measured. The separation between resonance and antiresonance frequencies is lowered with respect to the one simulated. The discrepancy in the quality factors measured for the resonators is even higher as they are about one order of magnitude lower than those calculated using the loss-less FEM simulation results. The quasi-2D FEM model takes into account bulk radiation as well as leakage of SAW across the mirrors that make up the cavity. Other possible loss mechanisms are SAW radiation leaking in the direction transverse to propagation (towards the buses), resistive losses in the transducer metallizations by Joule effect and finally viscoelastic losses in the gold metallizations. The length of the conduction lines connecting the electrodes to the G tips of the probe is not negligible so Joule losses likely have a non-negligible impact. However since gold is a relatively high conductivity material the majority of the attenuation is attributed to viscoelastic losses.

B. Proof of concept of a two state ladder SAW filter

In this section, the resonators studied in previous sections are used as impedance elements to fabricate ladder SAW filters and showcase their potential for fabrication of switchable SAW filters. The filters fabricated in this section are not switchable but rather frozen in order to make a first proof of concept with simple devices.

Impedance element SAW filters are a well known solution for achieving a pass-band response [27]. In the simplest configuration, referred to as an L cell, a parallel resonator is connected to a series resonator. Several cells can be cascaded

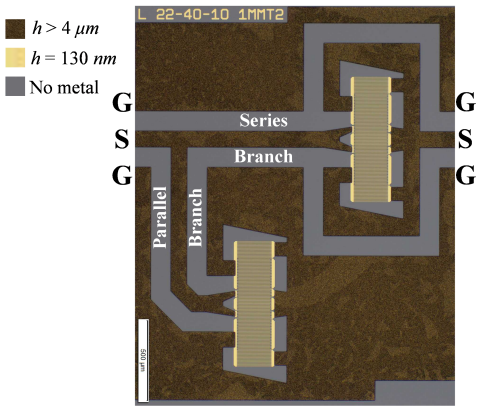

Fig. 13. Microscope image of a fabricated $[GG]^{11}[OG]^{20}[GT]^{5}[GO]^{8.5}$ condition single L cell filter. The placement of the GSG probes during measuring is denoted by the letters "GSG". The thickness of metallization in each zone of the device is visible thanks to the different colors as indicated in the legend.

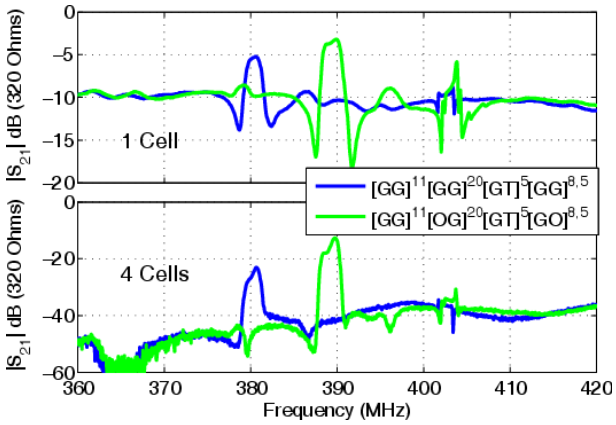

Fig. 14. Measured response for a 1 cell (a) and 4 cell (b) filters for electrical conditions $[GG]^{11}[GG]^{20}[GT]^{5}[GG]^{8.5}$ and $[GG]^{11}[OG]^{20}[GT]^{5}[GO]^{8.5}$, the measurements are performed using two 50 Ω GSG probes and the port impedance is changed to 320 Ω in post-processing.

to improve out of band rejection. For optimal operation, the resonance of the series resonator should occur at the same frequency as the anti-resonance of the parallel resonator. At this frequency, it can be shown that insertion losses depend on the ratio between the series and parallel impedances Z_s/Z_p and so lower series resonance impedance and higher parallel anti-resonance impedance are preferable. If the impedance at both ports of the filter is the same it can also be shown that the ideal port impedance is equal to the square root of the product of the series and parallel impedances at this frequency $\sqrt{Z_s Z_p}$.

Simulations show that by transforming the geometry of the resonator "Switch 1" through dimension scaling, the anti-resonance frequencies for both electrical conditions ($[GG]^{11}[GG]^{20}[GT]^{5}[GG]^{8.5}$ and $[GG]^{11}[1G]^{20}[GT]^{5}[1G]^{8.5}$) can be shifted such that a pass-band can be formed (even if these series resonance/parallel antiresonance frequencies don't perfectly match for both electrical conditions simultaneously). For a perfect geometry scaling to be carried out, the thickness of the electrodes should also be modified. However, the original thickness is kept at 130 nm for simplicity of fabrication while upscaling the period of the transducer and mirrors by a factor of 1.0047, which gives $p'_t = 4.762$ μm and $p'_m = 4.893$ μm. Ratios a'_t/p'_t and a'_m/p'_m are kept at 0.49 and 0.455, respectively. Since the dimensions of the electrodes are only marginally modified, the impact of the imperfect upscaling is also expected to be marginal besides the desired shift of the anti-resonance frequency of the resonator. For convenience (single metallization step in the fabrication process, and thus no dielectric bridge) $[GG]^{11}[1G]^{20}[GT]^{5}[1G]^{8.5}$ resonators are replaced by resonators with electrical condition $[GG]^{11}[OG]^{20}[GT]^{5}[GO]^{8.5}$. As discussed in section II-B.4, these two electrical conditions result in roughly the same resonator response. Fig. 13 presents a microscope image of a fabricated single cell L filter. In order to reduce resistive losses in the ground planes and coplanar waveguides, their thickness was increased to over 4 μm by electrolytic deposition. This can be seen in the figure by a brownish color due to surface roughness. In contrast, the resonator whose metallisations have a 130 nm thickness have a bright gold tint to them.

1-cell and 4-cell ladder filters are fabricated for each electrical condition of the mirrors. Measurement of the S parameter matrix of the filters is performed using two GSG probes and on post-processing the port impedance is changed from 50 Ω to 320 Ω, which was found to be close to the optimal impedance for both electrical conditions. Fig. 14 shows the resulting transmission (S_{21} parameter) in decibels for the 1 cell (a) and 4 cell (b) filters for both electrical conditions.

Main pass-bands centered at 380.5 and 389.7 MHz for the two electrical conditions are clearly visible, resulting in a 2.36 % relative frequency jump. The low quality factor of the resonators results in high insertion losses of between 3.22 and 5.3 dB per cell of the filter for both electrical conditions. Despite the electrolytic deposition the longer waveguides and ground planes likely still result in resistive losses. Finally, a weaker transmission peak can be spotted in all cases due to the SH resonance of the resonators around 404 MHz.

IV. Discussion

From these results on proof of concept tunable resonators and filters, several observations can be drawn. First, it should be pointed out that footprint reduction prospects remain moderate at this point, since the best scenario envisaged here would be a one cell tunable ladder filter with one switch per resonator to target two channels, to be compared with a switchable bank of two simple ladder filters. However, it is expected that more refined designs could lead to three or more pass-band options with, for instance, one operation point in-between the two demonstrated here. Each operating point corresponding to a different state of the electrodes making up the cavities, a higher number of switches would be needed but the reduction in footprint resulting from using a single filter instead of many would still be beneficial.

One important consideration that must be addressed is the integration of electronically controllable switches for commutation of the devices. MEMS switches or varactors [7] as well as VO_2 switches [14] present likely routes of inquiry.

Additionally, the question of the maximum achievable shift (i.e. channel separation) is also worth mentioning. In this type of system, it is related to both electrode reflectivity (i.e. coupling of SAW to the grating) and intrinsic electromechanical coupling. It should be noted that increasing the first parameter by mechanical means, for instance by increasing electrode thickness, is detrimental to the tunability potential, since the impact of the change in electrical conditions is then comparatively reduced. This adds an additional design constraint to the choice of substrate and electrode materials and geometries. However, it could be partially relaxed by exploiting the SAW regeneration effect with floating potential combs, which can introduce additional high reflection coefficient lobes of the mirror farther away from the GR and OC bandgaps. In any case, improved results could be found by transposing these results to state of the art multilayer substrates such as thin piezoelectric layers on Si [29], so called IHP multilayer substrates [15] or mono-crystalline substrates with Si overlayers [30]. Indeed $LiNbO_3$ YX/L 128º was only chosen due to availability in the lab and performance could be improved by picking a cut with higher electromechanical coupling.

Aigner concluded in his review that acoustic technologies due to high achievable quality factors would be of high interest for future telecommunications systems, but contrasted to SOI-CMOS devices they did not present an ease of tuning. Since the devices presented in this paper are subpar in terms of quality factor, practical tunable filters are still beyond our grasp. His definition of tunability was also broader than the application that the developed devices can achieve, a continuous frequency shift of the passband.

Nonetheless, the comparison between frozen and switchable devices presented (Fig. 11) shows a marginal impact on the electrical response due to the switching. This suggests that modification of electrode electrical conditions could be a promising avenue for tuning of electroacoustic filters without degrading the resonator quality factors.

Furthermore, nothing suggests that the subpar performance of the devices is inherent to the tuning but is rather a consequence of design choices and could be improved by utilizing a metal with lower mechanical dissipation, utilizing a substrate with higher electromechanical coupling and designing shorter devices, reducing the volume in vibration leading to less mechanical dissipation.

V. Conclusion

In this paper, the use of interdigitated combs set to different electrical conditions in order to design switchable SAW resonators and filters has been investigated. As a proof of concept, resonators with working frequencies around 400 MHz on $LiNbO_3$ substrate have been studied and fabricated. A relative frequency jump of around 2.2% of the main resonance has been realized. The switchable resonators were used to design a switchable ladder filter and frozen filters were fabricated, corresponding to the different electrical conditions of the resonators. Two port measurement results confirm that the frequency jumps attained for the resonators can be translated into similar jumps for filter pass-bands.

The resonators and filters used in this paper have not been optimized for performance but rather used as a proof of concept of the use of combs to design switchable SAW resonators. The next step for practical applications is to design resonators with better performance. For such an optimization, faster models such as mixed-matrix or coupling-of-modes approaches should be used [25], [28].

Finally, only single-port resonators were considered in this paper, but other SAW structures exist which could benefit from the use of comb mirrors. For example in two port longitudinally coupled resonator filters, finite sized gratings can be used to regulate coupling between the two ports [31]. Switchable couplers could also be used to allow for modification of the pass-band in this type of device.

Appendix

The material parameters used in the FEM simulations for $LiNbO_3$ YXL/128° are the following:

$$\rho = 4650(kg/m^3),$$

$$c_E = \begin{bmatrix} 198,39 & 53,53 & 66,31 & -6,95 & 0 & 0 \\ - & 208,99 & 80,49 & -6,09 & 0 & 0 \\ - & - & 186,56 & -6,31 & 0 & 0 \\ - & - & - & 75,01 & 0 & 0 \\ - & - & - & - & 74,86 & 4 \end{bmatrix} (GPa), \tag{4}$$

$$e_{ij}^T = \begin{bmatrix} 0 & 0 & 0 & 0 & -0,364 & 4,397 \\ 1,726 & 2,595 & -2,454 & -0,735 & 0 & 0 \\ 1,722 & 1,351 & -4,533 & 0,217 & 0 & 0 \end{bmatrix} (C/m^2), \tag{5}$$

$$\epsilon_{rS} = \begin{bmatrix} 45,537 & 0 & 0 \\ - & 33,566 & 9,353 \\ - & - & 38,230 \end{bmatrix}. \tag{6}$$

These material parameters differ slightly from constants found in the literature, for example those reported by Kovacs et al. [32]. Nonetheless as can be seen by comparing the simulation results and measurements they represent well enough the behaviour of the substrate. Gold is modelled as a cubic crystalline elastic material with parameters C_{11} = 186 GPa, C_{12} = 157 GPa, C_{44} = 42 GPa and a density of ρ = 19300 kg/m^3

Acknowledgment

The authors wish to thank Stéphane Xavier for the electron-beam lithography, as well as Éric Michouiller and Thierry Laroche from SOITEC for the fruitful discussions. This work was supported by the French Agence Nationale de la Recherche (FORMOSA Project No. ANR-18-ASMA-0003-01), the Agence Innovation Défense, and the Région Hauts-de-France.

REFERENCES

[1] R. Aigner. "Tunable Filters? Reality Check Foreseeable Trends in System Architecture for Tunable RF Filters". In: IEEE Microwave Magazine 16.7 (2015), pp. 82–88. DOI: 10.1109/MMM.2015.2428439.

[2] H. Zhou, A. Talbi, N. Tiercelin, and O. Bou Matar. "Multilayer magnetostrictive structure based surface acoustic wave devices". In: Applied Physics Letters 104.11 (2014), p. 114101. DOI:10.1063/1.4868530.

[3] S. Alzuaga, W. Daniau, R. Salut, T. Baron, S. Ballandras, and E. Defay. "Tunable and high quality factor $SrTiO_2$ surface acoustic wave resonator". In: Applied Physics Letters 105.6 (2014), p. 062901. DOI: 10.1063/1.4892659.

[4] R. Li, P. I. Reyes, S. Ragavendiran, H. Shen, and Y. Lu. "Tunable surface acoustic wave device based on acoustoelectric interaction in ZnO/GaN heterostructures". In: Applied Physics Letters 107.7 (2015), p. 073504. DOI: 10.1063/1.4928724.

[5] R. Li, G. Li, W.-C. Hong, P. I. Reyes, K. Tang, K. Yang, S.-Y. Wang, H. Ye, Y. Li, L. Zhang, K. Kisslinger, and Y. Lu. "Tunable surface acoustic wave device using semiconducting MgZnO and piezoelectric NiZnO dual-layer structure on glass". In: Smart Materials and Structures 27.8 (July 2018), p. 085025. DOI: 10.1088/1361-665X/aad006.

[6] R. Li, P. I. Reyes, G. Li, K. Tang, K. Yang, S.-Y. Wang, J. Han, N. W. Emanetoglu, and Y. Lu. "Tunable SAW Devices Based on Ni:ZnO/ZnO/GaN Structures with Buried IDTs". In: ECS Journal of Solid State Science and Technology 6.11 (Oct. 2017), S3119. DOI: 10.1149/2.0261711jss.

[7] K. Hashimoto, T. Kimura, T. Matsumura, H. Hirano, M. Kadota, and M. Esashi. "Moving Tunable Filters Forward: A Heterointegration Research Project for Tunable Filters Combining MEMS and RF SAW/BAW Technologies". In: Microwave Magazine, IEEE 16 (Aug. 2015), pp. 89–97. DOI: 10.1109/MMM.2015.2431237.

[8] K. Hashimoto, S. Tanaka and M. Esashi. "Tunable RF SAW/BAW filters: Dream or reality?" In : Proceedings of the IEEE International Frequency Control Symposium and Exposition (May 2011), pp. 1-8. DOI: 10.1109/FCS.2011.5977297

[9] M. Inaba, T. Omori, and K. Hashimoto. "A Configuration of Widely Tunable Surface Acoustic Wave Filter". In: Japanese Journal of Applied Physics 52.7S (June 2013), 07HD05. DOI: 10.7567/JJAP.52.07HD05. URL: https://dx.doi.org/10.7567/JJAP.52.07HD05.

[10] T. Wada, T. Ogami, A. Horita, H. Obiya, M. Koshino, M. Kawashima, and N. Nakajima. "A new tunable SAW filter circuit for reconfigurable RF". In: 2016 IEEE MTT-S International Microwave Symposium (IMS). 2016, pp. 1–4. DOI: 10.1109/MWSYM.2016.7540110.

[11] V. Gund, K. Nomoto, H. G. Xing, D. Jena, and A. Lal. "Intrinsically Switchable GHz Ferroelectric ScAlN SAW Resonators". In: 2022 IEEE International Symposium on Applications of Ferroelectrics (ISAF). 2022, pp. 1–4. DOI: 10.1109/ISAF51494.2022.9870089.

[12] M. Zolfagharloo Koohi, S. Lee, and A. Mortazawi. "Compact Intrinsically Switchable FBAR Filters Utilizing Ferroelectric BST". In: IEEE Transactions on Ultrasonics, Ferroelectrics, and Frequency Control 65.8 (2018), pp. 1468–1474. DOI: 10.1109/TUFFC.2018. 2839756.

[13] M. Zolfagharloo Koohi, S. Nam, and A. Mortazawi. "Intrinsically Switchable and Bandwidth Reconfigurable Ferroelectric Bulk Acoustic Wave Filters". In: IEEE Transactions on Ultrasonics, Ferroelectrics, and Frequency Control 67.5 (2020), pp. 1025–1032. DOI: 10.1109/TUFFC.2019.2958675.

[14] A. Fouladi Azarnaminy and Raafat R. Mansour. "Reconfigurable SAW Resonators and Tunable Filters Using Monolithically Integrated VO Switches". In: IEEE Transactions on Microwave Theory and Techniques 71.1 (2023), pp. 181–192. DOI: 10.1109/TMTT.2022.3222303.

[15] T. Takai, H. Iwamoto, Y. Takamine, T. Fuyutsume, T. Nakao, M. Hiramoto, T. Toi, and M. Koshino. "I.H.P. SAW technology and its application to microacoustic components (Invited)". In: 2017 IEEE International Ultrasonics Symposium (IUS). 2017, pp. 1–8. DOI: 10.1109/ULTSYM.2017.8091876.

[16] K. Hashimoto. "Chapter 7 : Coupling-of-Modes Theory". In: Surface acoustic wave devices in telecommunications. Modelling and simulation. Berlin, Germany: Springer, Jan. 2000, pp. 191–235. ISBN: 978-3-642-08659-5. DOI: 10.1007/978-3-662-04223-6.

[17] R. Alcorta Galván, C. Croënne, B. Dubus, B. Loiseaux, E. Eustache, M. Bertrand, and A.-C. Hladky-Hennion. "Switchability of a single port SAW resonator using the electrical Bragg band gap". In: Applied Physics Letters 120.20 (2022), p. 203504. DOI: 10.1063/5. 0093357. URL: https://doi.org/10.1063/5.0093357.

[18] D.P. Morgan. "Simplified analysis of surface acoustic wave one-port resonators". In: Electronics Letters 39 (Oct. 2003), pp. 1361–1362. DOI: 10.1049/el:20030851.

[19] K. Hashimoto, T. Omori, and M. Yamaguchi. "Design considerations on surface acoustic wave resonators with significant internal reflection in interdigital transducers". In: IEEE Transactions on Ultrasonics, Ferroelectrics, and Frequency Control 51.11 (2004), pp. 1394–1403. DOI: 10.1109/TUFFC.2004.1367478.

[20] S. Lehtonen, V. P. Plessky, C. S. Hartmann and M. M. Salomaa, "Unidirectional SAW transducer for gigahertz frequencies," in IEEE Transactions on Ultrasonics, Ferroelectrics, and Frequency Control, vol. 50, no. 11, pp. 1404-1406, Nov. 2003, doi: 10.1109/TUFFC.2003.1251122.

[21] P.V. Wright. "Low-cost high-performance resonator and coupled-resonator design: NSPUDT and other innovative structures". In: Proceedings of the 43rd Annual Symposium on Frequency Control 1992, pp. 574-587. DOI: 10.1109/FREQ.1989.68918.

[22] S. Degraeve, C. Granger, B. Dubus, J.O. Vasseur, M. Pham Thi, and A.-C. Hladky Hennion. "Bragg band gaps tunability in an homogeneous piezoelectric rod with periodic electrical boundary conditions". J. Appl. Phys. 21 May 2014; 115 (19): 194508. DOI:10.1063/1.4876757.

[23] G. Kovacs. "A generalised P-matrix model for SAW filters". In: IEEE Symposium on Ultrasonics, 2003. Vol. 1. 2003, 707–710 Vol.1. DOI: 10.1109/ULTSYM.2003.1293499.

[24] K. Hashimoto. Surface acoustic wave devices in telecommunications. Modelling and simulation. Springer-Verlag, Heidelberg, Jan. 2000, pp. 93–95. ISBN: 978-3-642-08659-5. DOI: 10.1007/978-3-662-04223-6.

[25] V. Plessky and J. Koskela. "Coupling-of-Mode analysis of SAW devices". In: International Journal of High Speed Electronics and Systems 10.04 (2000), pp. 867–947. DOI: 10.1142/S0129156400000684.

[26] C. Floer, S. Hage-Ali, P. Nicolay, H. Chambon, S. Zhgoon, A. Shvetsov, J. Streque, H. M'Jahed, and O. Elmazria. "SAW RFID Devices Using Connected IDTs as an Alternative to Conventional Reflectors for Harsh Environments". In: IEEE Transactions on Ultrasonics, Ferroelectrics, and Frequency Control 67.6 (2020), pp. 1267–1274. DOI: 10.1109/TUFFC.2019.2943310.

[27] J. Heighway, S.N. Kondratyev, and V.P. Plessky. "Impedance element SAW filters". In: Proceedings of IEEE 48th Annual Symposium on Frequency Control. 1994, pp. 374–378. DOI: 10.1109/FREQ.1994.398309.

[28] P. Ventura, J.M. Hode, M. Solal, J. Desbois, and J. Ribbe. "Numerical methods for SAW propagation characterization". In: vol. 1. Feb. 1998, 175–186 vol.1. ISBN: 0-7803-4095-7. DOI: 10.1109/ULTSYM.1998.762125.

[29] E. Butaud, S. Ballandras, M. Bousquet, A. Drouin, B. Tavel, I. Huyet, A. Clairet, I. Bertrand, A. Ghorbel, and A. Reinhardt. "Innovative Smart Cut™ Piezo On Insulator (POI) Substrates for 5G acoustic filters". In: 2020 IEEE International Electron Devices Meeting (IEDM). 2020, pp. 34.6.1–34.6.4. DOI: 10.1109/IEDM13553.2020.9372020.

[30] B. Abbott, A. Chen, T. Daniel, K. Gamble, T. Kook, M. Solal, K. Steiner, R. Aigner, S. Malocha, C. Hella, M. Gallagher, and J. Kuypers. "Temperature compensated saw with high quality factor". In: 2017 IEEE International Ultrasonics Symposium (IUS). 2017, pp. 1–7. DOI: 10.1109/ULTSYM.2017.8092294.

[31] K. Nakamura and H. Amano. "Design of longitudinally coupled SAW resonator filters with Chebyshev characteristics". In: Proceedings of 1996 IEEE International Frequency Control Symposium. 1996, pp. 273–277. DOI: 10.1109/FREQ.1996.559866.

[32] G. Kovacs, M. Anhorn, H.E. Engan, G. Visintini, and C.C.W. Ruppel. "Improved material constants for $LiNbO_3$ and $LiTaO_3$". In: IEEE Symposium on Ultrasonics. Vol. 1. 1990, pp. 435–438. DOI: 10.1109/ULTSYM.1990.171403.

[33] D.A. Feld, R. Parker, R. Ruby, P. Bradley, and S. Dong. "After 60 years: A new formula for computing quality factor is warranted". In: 2008 IEEE Ultrasonics Symposium, pp. 431-436. DOI: 10.1109/ULTSYM.2008.0105.